The International Journal of Advanced Manufacturing Technology (2018) 98:2611–2618
https://doi.org/10.1007/s00170-018-2408-9

ORIGINAL ARTICLE

Modeling of thermal cycles and microstructural analysis of pipeline steels processed by friction stir processing

J. A. Avila[1] · R. A. R. Giorjao[2,3] · J. Rodriguez[4] · E. B. Fonseca[5] · A. J. Ramirez[6]

Received: 4 April 2018 / Accepted: 9 July 2018 / Published online: 17 July 2018

Abstract
During friction stir welding or processing (FSP), temperature and deformation have influence on the final microstructure and mechanical properties. Studying microstructures before and after welding might help interpreting mechanical and corrosion resistance; however, microstructural evolution during the process remains unknown. In this study, a FSP model of pipeline steel plates was developed. Thermocouples were inserted in different positions and temperature cycles were collected during FSP. The collected data was used to complete the numerical model based on computational fluid dynamics (CFD). The CFD model simulated the material flow and heat transfer in FSP considering the material as a fluid. The standard error between the peak temperatures of the simulation and experimental results was below 1%. The model allowed correlating peak temperatures and cooling rates to the obtained microstructures after FSP. Numerical results showed that peak temperatures and dwell times in the stir zone were high enough to cause grain coarsening. This observation was demonstrated upon prior-austenite grain size measurements.

Keywords Computational fluid dynamics · Friction stir processing · Friction stir welding · Pipeline steel · Numerical modeling · Microstructural analysis

1 Introduction

Friction stir welding (FSW) or processing (FSP) in high-strength low-alloy (HSLA) steels is a promising technology in the pipeline construction industry [1–4] and shipbuilding industry [5]. FSW can perform welded joints of thick sections with one or multiple passes and causes little loss in mechanical properties and toughness [1–5]. During FSW, there is no melting of the workpiece nor the welding tool. The heat source in FSW considers the influence of the tool threads on the material flow [6], friction and plastic deformation of the interface between the tool and the workpiece, and the plastic deformation in the thermomechanically affected zone (TMAZ) [7–9]. At the end of the process, a coalesced joint between two plates or a reprocessed material is obtained.

FSW in HSLA steels presents lower peak temperatures, smaller distortion of the workpiece, and grain coarsening within the welded zone than fusion welding [5]. The highest processing temperatures above 1200 °C have been reported for FSW joints in HSLA steels [4, 10–13]. Cooling rates have been reported between 20 and 240 °C s^{-1} for the stir zone (SZ) and hard zone (HZ) [14]. HZ is usually found in the advancing side and the top side close to the centerline of the joint [15]. HZ exhibits higher hardness than the rest of the SZ; therefore, it is supposed that HZ presents higher peak temperatures and cooling rates than the rest of the SZ [15, 16]. Peak temperatures above 1150 °C with heating rates of 10 and 100 °C s^{-1} caused austenite coarsening of approximately 20 μm in a X80 pipeline steel [17]. Therefore, FSW may lead to the formation

✉ J. A. Avila
julian.avila@unesp.br

[1] São Paulo State University (UNESP), Campus de São João da Boa Vista, Av. Profª Isette Corrêa Fontão, 505, Jardim das Flores, São João da Boa Vista, SP 13876-750, Brazil

[2] Brazilian Nanotechnology National Laboratory, Rua Giuseppe Máximo Scolfaro 10000, Campinas, SP 13083970, Brazil

[3] Department of Metallurgical and Materials Engineering, University of São Paulo (USP), São Paulo, SP 05508-900, Brazil

[4] EIA University, Km 2 + 200 Vía al Aeropuerto José María Córdova, Envigado 055428, Antioquia, Colombia

[5] School of Mechanical Engineering, University of Campinas, Rua Mendeleyev 200, Campinas, SP, Brazil

[6] The Ohio State University, 1248 Arthur E. Adams Drive, Columbus, OH 43221, USA

of coarse microstructure due the high peak temperatures, and bainite packets with irregular and straight ferrite plates within the SZ and HZ because the rapid cooling rates [1].

Good mechanical properties and high toughness have been found for FSW joints in HSLA steels [1]; however, there are still questions to be addressed, such as factors affecting the post-processing microstructure and mechanical behavior, e.g., dynamic recrystallization, precipitation, and coarsening, that depends on temperature and deformation during processing [18]. Microstructural evolution during FSW was not fully understood because no physical means to directly measure the deformation conditions—especially strain and strain rate—has been achieved yet. However, a few methods have been suggested to indirectly measure or estimate these conditions. Physical simulation, for example, can reproduce microstructures of FSW joints according to the starting and ending stages [12]. This method not necessarily reproduces the microstructural evolution but provides hints of the transformation products and thermal cycles during processing. Another method is the thermomechanical computational fluid dynamic modeling. In CFD numerical model, the basic concept is to consider the material as a high-viscosity fluid. The heat in the process is mainly generated from viscous dissipation and frictional sliding in the contact region between the tool and the workpiece and is controlled by a spatial sticking-sliding parameter based on the tool radius. The model is useful to predict the welding-affected zones and to provide thermal cycle evolution during FSW [19, 20]. Thus, by merging computational modeling with post-processed microstructural analysis, a better understanding of FSP can be reached.

Several studies using CFD have attempted to model FSW in steels. However, various aspects regarding coarse bainite formation at the stir zone of pipeline steels remain unresolved. In the present study, a CFD model based on thermal cycles measured during FSP was used to analyze post-processed microstructures. Thus, we correlated peak temperatures and cooling rates with the available literature to understand better the obtained microstructures after FSP. For this purpose, we used electron microscopy coupled with an electron backscattering diffraction (EBSD) detector for microstructure characterization. Prior-austenite grain sizes (PAGS) were measured with etched samples and reconstruction of parent grains from EBSD data.

2 Experimental procedure

In a previous research, toughness impact and microstructural characterization were successfully performed in 15-mm-thick friction stir-processed plates [2]. In that study, the ductile to brittle temperature was determined for several microstructural regions of the FSP pass, finding low toughness at the stir and hard zone, due to the presence of the large bainite packages in these regions. In addition, to avoid large machining of channels and holes to position thermocouples, we now use a thinner plate (9.5 mm) to perform thermal cycles measurements to provide information to the numerical modeling. Results allowed us to understand better the microstructural evolution in the SZ and HZ. Difference in thickness at the CFD was easily resolved.

We also noticed that FSW butt joints and FSP of HSLA steels with the same thickness, using the same parameters and tool, will provide similar macro- and microstructures, as proved with results of previous research [1, 2]. Therefore, in exploratory studies, FSP is a material-saving procedure and is much more advantageous than FSW.

2.1 Material, temperature measurements, and welding parameters

At the present study, two plates of API-5L X80 pipeline steel with thicknesses of 15 mm and 9.5 mm and areas of 100 × 400 mm^2 were used to produce a processed pass in each plate. The mechanical properties of the plates, as determined in a previous study [2], are yield strength of 593 ± 21 MPa, tensile strength of 658 ± 34, and elongation of 17 ± 1%. The chemical composition of the plates is shown in Table 1.

Based on previous research [1, 2], the processing parameters and tool were selected. Figure 1b shows the step-spiral PCBN-WRe tool, with conical shape and 9.5-mm pin length used in both plates. Average welding parameters were spindle speed (ω) of 300 rev min^{-1}, travel speed (ν) of 100 mm min^{-1}, spindle torque (τ_q) of 115 N m, and downward force (F_z) of 34 kN [2]. The heat input (HI) was determined using Eq. 1 [21] that considers the welding parameters.

$$HI = \frac{2\pi\omega\tau_q}{1000\nu} \left[\text{kJ mm}^{-1}\right] \quad (1)$$

The first plate, 9.5 mm thick, was used to acquire the thermal cycle in various positions along the welded joint. K-type thermocouples with a 0.5-mm diameter were welded in specific positions of the plate, according to Fig. 1a and Table 2. Holes with 4 mm in diameter were machined on the plates to place the thermocouples.

Table 1 Chemical composition of API 5L X80 steel (wt%). *CE* P_{cm} carbon equivalent. *ppm [2]

C	Si	Mn	Mo	Nb	Ni	P*	Ti	V	N*	B*	S*	CE P_{cm}
0.04	0.32	1.56	0.19	0.03	0.24	< 100	0.01	0.01	< 6	5	60	0.15

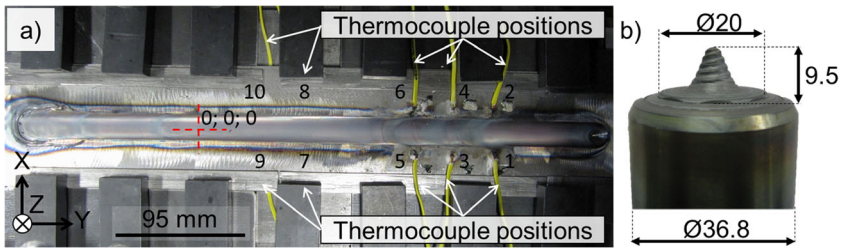

Fig. 1 **a** Thermocouple positions at the processed plate; **b** tool geometry and dimensions. The coordinate 0; 0; 0 represents the center location for the thermocouple positioning

Usually, in similar processing pass [2], the first 25 mm undergoes transient behavior; thus, thermocouples were placed from the second quarter of the FSP length onwards. The second plate, 15 mm thick and without any thermocouples attached, provided the metallography samples.

Thermal cycles were acquired with thermocouples attached in positions close to the heat-affected zone (HAZ). This thermal history was processed and used into the numerical model. Thermocouples located in the tool path were not used because of inefficient measurements. For the numerical model, experimental data and thermal cycles in different regions during friction stir welding were conducted.

Optical microscopy and SEM coupled with an EBSD detector were used to perform microstructural characterization. EBSD maps were acquired at 20 kV and step size between 0.08 and 0.2 μm. Aztec HKL from Oxford Instruments software, Channel 5-Tango, was used for indexing and post-processing EBSD maps. An automatic reconstruction of parent grains (*ARPGE*) [22] software was used to process prior-austenite grains. The ARPGE software uses symmetry and probability operators; then, parent grains (prior-austenite) are reconstructed from daughter data (bainite packages, ferrite) [22].

Metallography specimens were grounded and polished up to colloidal silica. Nital 3% and ammonium persulfate etching [23] were used to reveal conventional grain boundaries and prior-austenite grain boundaries, respectively. No etching procedure was used before EBSD analysis.

2.2 Numerical simulation

A computational fluid dynamics (CFD) three-dimensional steady-state modeling was performed using finite element Comsol multi-physics v5.1 software, which was based on a previous model [3]. The heat generation and material flow model was based on models proposed by Nandan [7] and Schmidt et al. [9]. Our model accepts an imperfect contact between the steel plates and the backing plate, with contact resistance of 1000 $mm^2\ K\ W^{-1}$ [6]. Room temperature (23 °C) was set on the bottom of the backing plate. A convective heat transfer coefficient of 20 $W\ m^{-2}$ K was used as loss from the top surface of the workpiece.

Viscosity considered for the CFD model was based on the Zener-Holloman equation (Eqs. 2–4), during material flow, which relates the flow of the material with temperature and strain rates [24, 25]. A, n, Q_{def}, and α are constants for the model calculations [26], with values of 5.1 for n, 387 kJ mol^{-1} for Q, and $1.91 \cdot 10^{19}$ for A. Variations of the thermal properties with the temperature, such as thermal conductivity and heat capacity used in the model, were calculated and reported elsewhere [27].

$$\mu = \frac{\sigma_e}{3\dot{\epsilon}} \tag{2}$$

$$\dot{\epsilon} = A(\sinh\alpha\sigma)^n \exp\left(-\frac{Q_{\text{def}}}{RT}\right) \tag{3}$$

Table 2 Thermocouple positions within the welded joint. *AS*, advancing side; *RS*, retreating side

Thermocouple no.	Depth from the top surface (mm)	Lateral distance from the weld center line (mm); AS (−) and RS (+)
1	2.40	+ 13
2	2.42	− 13
3	2.44	+ 16
4	2.47	− 16
5	0.00	+ 13
6	2.46	− 13
7	5.36	+ 12
8	5.32	− 12
9	3.33	+ 14
10	3.29	− 14

$$\sigma_e = \frac{1}{\alpha}\, sinh^{-1}\left[\left(\frac{Z}{A}\right)^{\frac{1}{n}}\right] \tag{4}$$

Two sources of heat were considered: heat generation at the tool/workpiece interface and due to the material plastic deformation [7, 28]. The interface heat generation is described by Eq. 5, where r_{pin} is the radius of the pin, ω is the spindle speed, δ is the stick-slip coefficient, μ the friction coefficient, τ is the flow stress of the material, and p is the pressure applied by the downward force of the tool. The stick-slip coefficient applied in the model was 0.7, also used in simulations by Nandan [7].

$$q_{\text{at}} = [\delta\tau + (1-\delta)\mu p]\left(r_{pin}\omega - U sin\theta\right)dA, \quad T < Solidus\ q_{at} = 0, \quad T \geq Solidus \tag{5}$$

The heat generated by the plastic deformation can be estimated by the ratio between the velocity fields of the material during the process. The simplified equation used by Nandan [7] is described in Eq. 6 as follows:

$$q_{def} = \beta_{\text{h}}\mu\varphi\, dV \tag{6}$$

where β_{h} is the energy fraction generated by the heat dissipation in the form of heat and φ is given by Eq. 7, where x_i is the space dimension:

$$\varphi = 2\Sigma_{i=1}^{3}\left(\frac{\partial u_i}{\partial x_i}\right)^2 + \left(\frac{\partial u_1}{\partial x_2} + \frac{\partial u_2}{\partial x_1}\right)^2 + \left(\frac{\partial u_1}{\partial x_3} + \frac{\partial u_3}{\partial x_1}\right)^2 + \left(\frac{\partial u_3}{\partial x_2} + \frac{\partial u_2}{\partial x_3}\right)^2 \tag{7}$$

The simulation was made assuming steady-state conditions, to avoid instabilities caused by the plunge and extract of the tool. Welding parameters for the simulations were constant, such as axial force (34 kN), spindle speed (300 rev min^{-1}), and welding speed (100 mm min^{-1}). Tetragonal elements with smaller sizes (ranging from 2 to 20 mm) in the regions near the tool than the rest of the workpiece were used at the mesh. The thermal model was adjusted using the thermal cycles acquired during welding. Experimental data from 9.5-mm-thick plates was used to validate the model. Then, the model was used to estimate the temperature distribution in the 15-mm-thick plates. In addition, temperature correlations between the thermal cycle and microstructures of the welded joint in 15-mm-thick plate were made.

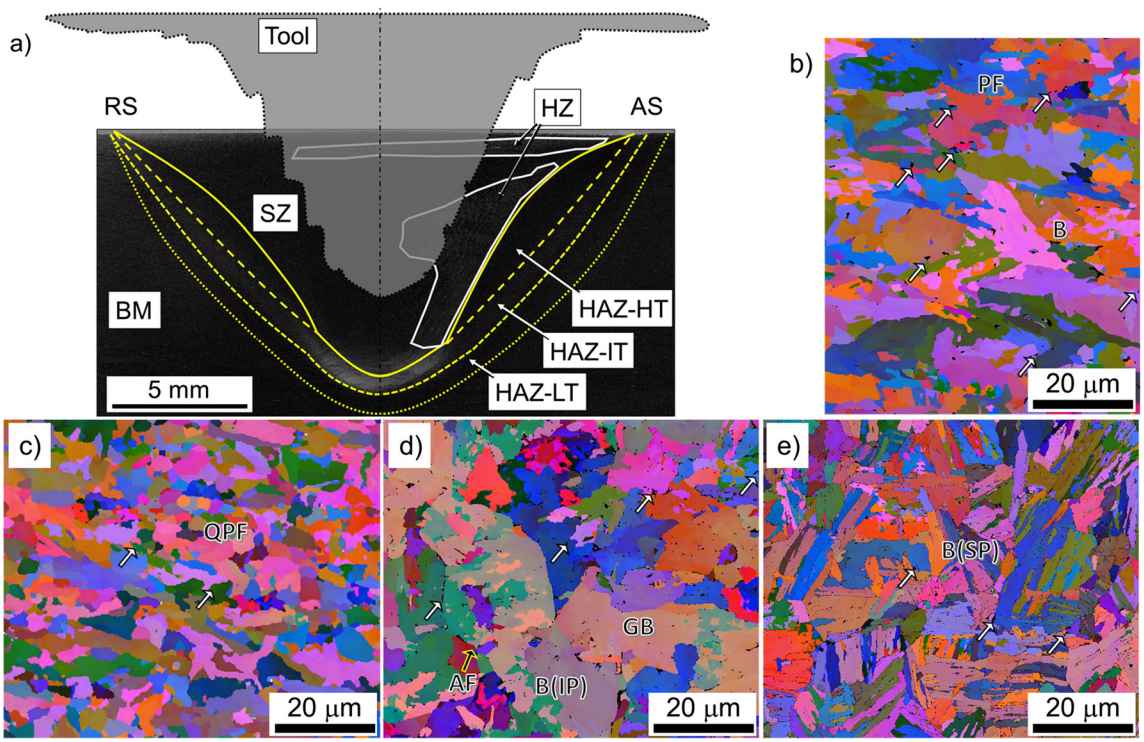

Fig. 2 **a** Cross-sectional view of a 15-mm-thick plate showing macrostructure of FSP using a 9.5-mm pin tool. Optical microscopy, Nital 3% etching. EBSD maps of **b** base metal (BM), **c** heat-affected zone (HAZ), **d** stir zone (SZ), and **e** hard zone (HZ). HAZ-HT, HAZ high temperature; HAZ-IT, HAZ intermediate temperature; HAZ-LT, HAZ low temperature; RS, retreating side; AS, advancing side. Microstructures: polygonal ferrite (PF), quasi-polygonal ferrite (QPF), acicular ferrite (AF), bainite (B), granular bainite (GB), bainite with irregular plates (B-IP), bainite with straight plates (B-SP), and fine secondary phases pointed with the white arrows

3 Results and discussion

3.1 Macro- and microstructural features

Figure 2 shows the macrostructural zones and their approximate boundaries, and microstructures at the base metal (BM), HAZ, SZ, and HZ. A conical and step-spiral tool schema was placed in the same figure. The tool was displaced upwards of the real working position, to illustrate the material affected by processing.

Microstructure of BM was mainly polygonal ferrite (PF) and small amount of bainite (B) [2] (Fig. 2b). HAZ was divided into three regions regarding the microstructure, hardness [2], and HAZ regions proposed by Lienert et al. [10]: high- (above 900 °C, HAZ-HT), intermediate- (approx. 700–900 °C, HAZ-IT) and low- (below 700 °C, HAZ-LT) temperature zones. The HAZ, as shown in Fig. 2c, exhibited mainly quasi-polygonal ferrite (QPF) as the main microstructure. SZ, shown in Fig. 2d, is the largest zone modified by FSP and exhibited acicular ferrite (AF) and mainly polygonal bainite packets with irregular ferrite grains [B(IP)]. However, the hard zone (HZ), located at the right side within the SZ, as shown in Fig. 2e depicted elongated bainite packets with straight ferrite plates [B(SP)].

3.2 Experimental and modeling thermal cycles comparison

Except for thermocouples identified as 3, 4, 5, and 6 in Table 1, broken during the experimental data acquisition, the other sites worked properly. Experimental and simulated thermal cycles were plotted in Fig. 3. Experimental results show that peak temperatures were slightly higher at the advancing side than at the retreating side. The peak temperature increases as the distance from the weld center decreases, for both sides. The standard error between the peak temperatures of the simulation and experimental results was below 1%. Therefore, the numerical simulation successfully agrees with the experimental data.

3.3 Numerical simulation analysis

The numerical simulation was used to study the peak temperatures, cooling rates, and dwell times of the material during friction stir processing. Figure 4a indicates the macrostructural zones analyzed by the simulation: SZ, HZ, and HAZ. Streamlines passing throughout the HAZ, SZ, and HZ were simulated with particles. The temperature profile of each particle was plotted in Fig. 4b and thermal cycles in Fig. 4c.

According to the thermal cycle of the particles, dwell times above complete austenitization temperature, A3 ~ 900 °C [27], were 6.9 s., 5.3 s, 5.1 s, and 3.8 s at HZ, SZ, SZ-RS, and HAZ-AS, respectively. In addition, peak temperature was slightly higher at HZ than SZ, and SZ than HAZ. Therefore, long exposure time and high peak temperatures might be the cause of the largest coarsening in HZ. The simulated cooling rates at the stir zone were different from the advancing to the retreating sides, with differences around 4 °C s^{-1} between opposing sites, similar to the model stated by De et al. [29], who reported no significantly differences throughout the stir zone.

Post-welding cooling rates have been reported as the main factor controlling microstructures through the SZ [14, 15]. However, based on the numerical simulation, cooling rate difference between HZ and HAZ-RS was only 6.3 °C s^{-1}, which seems not enough to cause substantial changes in the microstructure at the different zones. Furthermore, within the welded zone, peak temperatures are higher than those at the HAZ, and the peak temperature at the HZ is the highest.

EBSD inverse pole figure (IPF) maps and austenitic grain size reconstruction (ARPGE software) are shown in Fig. 5 for

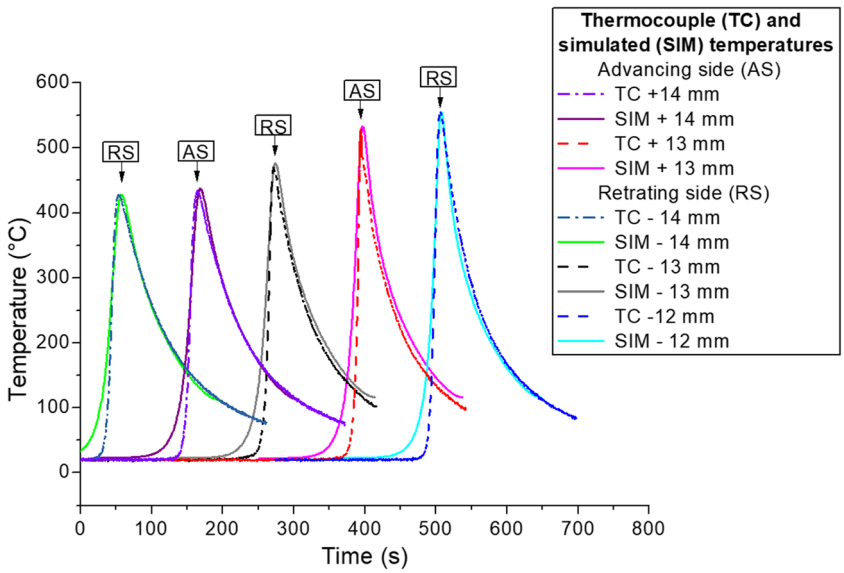

Fig. 3 Experimental and simulated thermal cycles comparison: temperature versus time. Experimental thermal cycles were measured using thermocouples at the 9.5-mm-thick friction stir-processed (FSP) plate. Experimental results are shown with solid (TC) and simulated results with dashed lines (SIM)

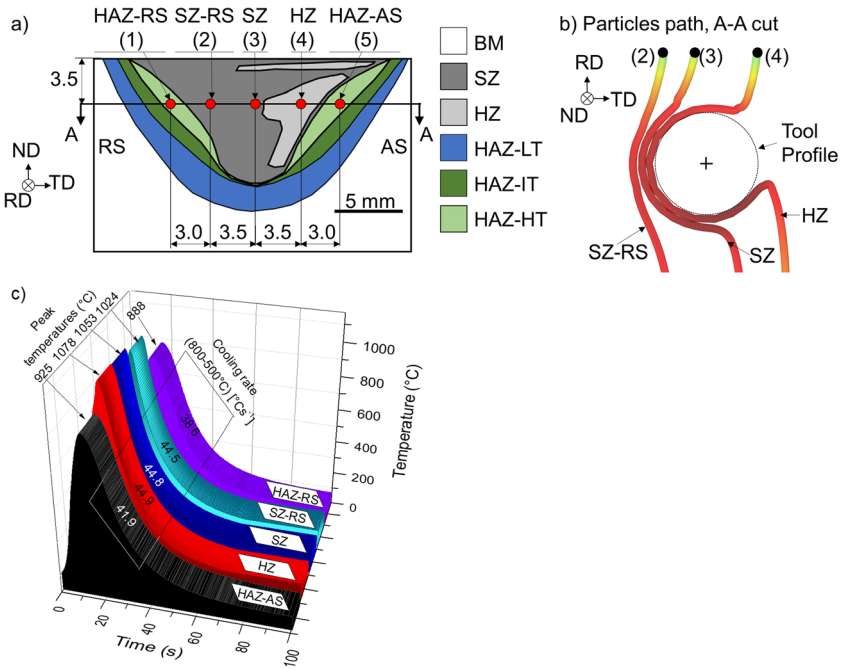

Fig. 4 Simulated thermal cycles in specific locations of the 9.5-mm-thick friction stir-processed (FSP) plate. **a** Cross section of the weld showing the macrostructural zones, **b** particle trajectories at given positions, and **c** thermal cycles. BM, base metal; HAZ, heat-affected zone; HAZ-HT, HAZ of high temperature; HAZ-IT, HAZ of intermediate temperature; HAZ-LT, HAZ of low temperature; SZ, stir zone; HZ, hard zone; RS, retreating side; AS, advancing side. Directions: rolling (RD), transversal (TD), and normal (ND)

the BM, SZ, and HZ. Figure 6 shows comparison between PAGS measurements conducted with the ARPGE reconstructions and from optical grain size measurements. The largest PAGS were found at the HZ, where the highest peak temperature took place. The HZ, SZ, and SZ-RS exhibited different cooling rates, as shown in Fig. 4c, which also correspond to the different microstructures found in these regions [2]. Therefore, in HZ and SZ, the cooling rate, dwell time, and peak temperature around 1150 °C allowed the coarsening of the austenite and its decomposition in bainite products, where the HZ displayed straighter ferrite products than SZ.

4 Discussion

In a previous study, cooling rates of 150 °C s^{-1} between the advancing and retreating sides were reported [14]. However, according to our numerical simulation, it is unlikely that such a significant difference in cooling rates exists in such a small distance. In addition, Nelson et al. [15] reported that cooling rates below 20 °C s^{-1} eliminated the presence of the hard zone, while we found the same microstructures up to around 45 °C s^{-1}. Difference between our FSW modeling results and the open literature [14, 15] is related to chemical composition of the steels, thermal and strain history before processing or welding, and welding parameters. Therefore, taking into account the material flow and thermal history dependency on the metallurgical aspects of the workpiece [30], tool design, and type of material [4] is important to better interpret the produced microstructures and its evolution.

Austenite coarsening was observed at the stir zone, as it increases with the peak temperature, which was similarly reported in several studies of FSW in HSLA steels [4, 10, 14, 31] and carbon steels [32]. It is also in agreement with the austenite grain growth model performed in a X80 steel [17] that presents a similar chemical composition to the one used at the present paper. This study revealed a slow grain growth from 6 μm at 950 °C to 15 μm at 1150 °C. Above 1150 °C,

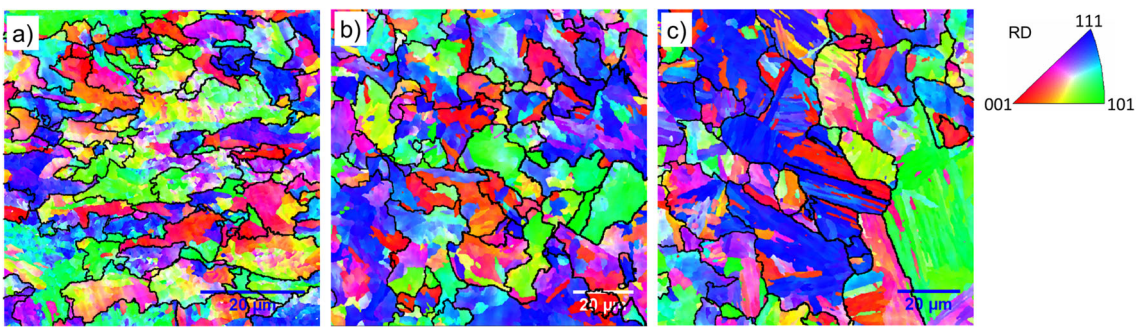

Fig. 5 EBSD inverse pole figure (IPF) maps with the *ARPGE* reconstructed prior austenite grains boundaries: **a** base metal, **b** stir zone, and **c** hard zone

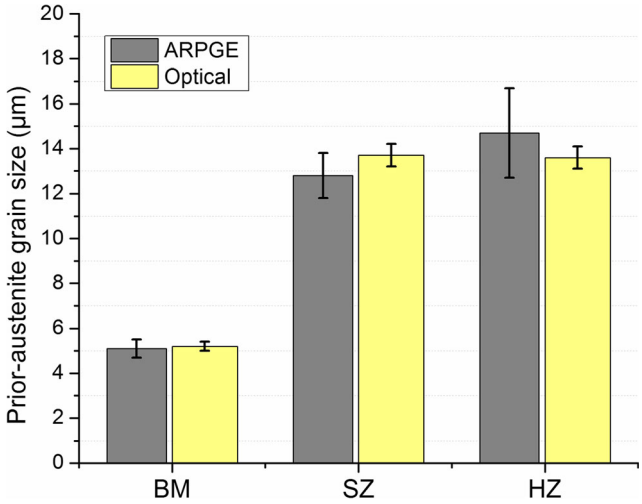

Fig. 6 Prior-austenite grain size of *ARPGE* reconstruction and optical measurements

the grain growth is accelerated by fast dissolution of precipitates, which reduces the pinning effect [17] and cannot avoid boundaries migration. Therefore, that slight difference in peak temperature and coarsening of the austenite between the SZ and HZ must have accounted for the hardness increase and the straightening of the bainite packages within the HZ.

Post-processing microstructures at FSW are complex due to the differentiated strain and thermal cycles conducted at the material by the tool during the metal stirring, as observed in the CFD and reported by other authors [4, 11]. In addition, subsequent cooling rates had a fundamental role favoring the formation of lath microstructures and increasing hardening, also depicted in the literature [12–14]. As a result, a microstructural mixing of polygonal ferrite (PF), quasi-polygonal ferrite (QPF), acicular ferrite (AF), granular bainite (GB), bainite with irregular plates (B-IP), bainite with straight plates (B-SP), and fine secondary phases [6] can be observed in FSW passes [2]. Other important events happening in high temperatures are the dynamic recrystallization (DRX) and precipitation, two competing phenomena that might affect the coarsening of austenite grains [17, 18, 33] and hardening. Due to plastic deformation during FSW, defects are generated, and energy is stored in the microstructure. This stored energy is much higher in a FSW than in a conventional hot rolling process [29], for example. In addition, the stored energy varies according to the analyzed position within the welded joint and might be related to the particles trajectory, as shown in Fig. 4b. Furthermore, deformation in high temperature as presented by FSP affects phase transformation and produces complex microstructures.

In previous research of HSLA steels of similar type [1, 2], HAZ presented better toughness than SZ and HZ, and SZ than HZ, which is directly related to the microstructure products found in each region. For instance, SZ and HZ shared several features with the coarse-grained HAZ (CGHAZ) in fusion welds [34], e.g., coarse microstructure and brittle zones. Despite deleterious effect of PAGS growth in toughness, FSW produces less coarsening than fusion welding, e.g., in the stir zone was found PAGS around 15 μm, and heat-affected zone of fusion welding has been reported between 75 and 150 μm [2]. In addition, the necklace formation of martensite-austenite (M-A) constituent [35] normally found at the second pass of the intercritically reheated coarse-grained HAZ (ICCGHAZ) in fusion welds is absent in the FSW microstructures, which definitely improve mechanical properties and toughness of FSW joints in comparison to fusion welding.

5 Conclusions

- The numerical simulation of FSW successfully followed experimental measurements at the heat-affected zone and allowed correlation of peak temperatures, cooling rates, and the FSW post-processed microstructures in a HSLA steel (X80).
- The coarsening of the microstructure at the SZ and HZ and straightening of ferrite plates on the bainite packages at HZ was associated to high peak temperatures (above 1150 °C), long dwell times, and cooling rates above 20 °C s^{-1}.
- Austenite grain reconstruction and optical measurements aided distinguishing prior-austenite grain sizes between the stir and hard zones, which was well correlated to thermal cycles, the numerical model of FSW and literature models of the austenite grain growth.
- Controlling peak temperatures below 1150 °C and cooling rates to avoid straight plates of ferrite formation might allow refining the microstructure at the stir and hard zone, furthermore, mechanical properties may be improved.

Acknowledgements The authors would like to thank the LNNano for the provision of the FEI ® Quanta 650FEG SEM/EBSD microscope, FSW machine, and metallography facilities; PETROBRAS for providing economic funding; and Tenaris Confab for the material donation.

References

1. Avila JA, Rodriguez J, Mei PR, Ramirez AJ (2016) Microstructure and fracture toughness of multipass friction stir welded joints of API-5L-X80 steel plates. Mater Sci Eng A 673:257–265. https://doi.org/10.1016/j.msea.2016.07.045
2. Avila JAD, Lucon E, Sowards JW et al (2016) Assessment of ductile-to-brittle transition behavior of localized microstructural regions in a friction-stir welded X80 pipeline steel with miniaturized Charpy V-notch testing. Metall Mater Trans A 47:2855–2865. https://doi.org/10.1007/s11661-016-3473-z

3. Hoyos JJ, Pereira VF, Giorjao RR et al (2016) Effect of friction stir welding on hydrogen content of ISO 3183 X80M steel. J Manuf Process 22:82–89. https://doi.org/10.1016/j.jmapro.2016.01.012
4. Fairchild DP, Kumar A, Ford SJ, et al (2009) Research concerning the friction stir welding of linepipe steels. In: Trends in welding research, 8th International Conference. pp 371–380
5. McPherson N, Galloway M, Cater SR, Hambling SJ (2013) Friction stir welding of thin DH36 steel plate. Sci Technol Weld Join 18:441–450. https://doi.org/10.1179/1362171813Y.0000000122
6. Colegrove PA, Shercliff HR (2005) 3-Dimensional CFD modelling of flow round a threaded friction stir welding tool profile. J Mater Process Technol 169:320–327. https://doi.org/10.1016/j.jmatprotec.2005.03.015
7. Nandan R (2008) Computational modeling of heat transfer and visco-plastic flow in friction stir welding. The Pennsylvania State University
8. Simar A, Lecomte-Beckers J, Pardoen T, de Meester B (2006) Effect of boundary conditions and heat source distribution on temperature distribution in friction stir welding. Sci Technol Weld Join 11:170–177. https://doi.org/10.1179/174329306X84409
9. Schmidt H, Hattel J, Wert J (2004) An analytical model for the heat generation in friction stir welding. Model Simul Mater Sci Eng 12:143–157. https://doi.org/10.1088/0965-0393/12/1/013
10. Lienert TJ, Stellwag WL, Grimmett BB, Warke RW (2003) Friction stir welding studies on mild steel. Weld J 82(1):1–9
11. Barnes SJ, Steuwer A, Mahawish S et al (2008) Residual strains and microstructure development in single and sequential double sided friction stir welds in RQT-701 steel. Mater Sci Eng A 492:35–44. https://doi.org/10.1016/j.msea.2008.02.049
12. Sinfield MF (2007) Advancements in physical simulation and thermal history acquisition techniques for ferrous alloy friction stir welding. The Ohio State University
13. Norton SJ (2006) Ferrous friction stir weld physical simulation. The Ohio State University
14. Allred J (2013) An investigation into the mechanisms of formation of the hard zone in FSW X65. Brigham Young University
15. Nelson TW, Rose S (2016) Controlling hard zone formation in friction stir processed HSLA steel. J Mater Process Technol 231:66–74. https://doi.org/10.1016/j.jmatprotec.2015.12.013
16. Ozekcin A, Jin HW, Koo JY et al (2004) A microstructural study of friction stir welded joints of carbon steels. Int J Offshore Polar Eng 14:284–288
17. Banerjee K, Militzer M, Perez M, Wang X (2010) Nonisothermal austenite grain growth kinetics in a microalloyed x80 linepipe steel. Metall Mater Trans A 41:3161–3172. https://doi.org/10.1007/s11661-010-0376-2
18. McQueen HJ, Yue S, Ryan ND, Fry E (1995) Hot working characteristics of steels in austenitic state. J Mater Process Technol 53:293–310. https://doi.org/10.1016/0924-0136(95)01987-P
19. Kumar A, Fairchild DP, Anderson TD, et al (2010) Research progress on friction stir welding of pipeline steels. In: International Pipeline Conference. pp 1–9
20. Almoussawi M, Smith AJ, Young A et al (2017) Modelling of friction stir welding of DH36 steel. Int J Adv Manuf Technol 92:341–360. https://doi.org/10.1007/s00170-017-0147-y
21. Kyffin WJ (2007) FSW as a repair technique for surface cracks in stainless steel. Cambridge
22. Cayron C (2007) ARPGE: a computer program to automatically reconstruct the parent grains from electron backscatter diffraction data. J Appl Crystallogr 40:1183–1188. https://doi.org/10.1107/S0021889807048777
23. Reiter J, Bernhard C, Presslinger H (2008) Austenite grain size in the continuous casting process: metallographic methods and evaluation. Mater Charact 59:737–746. https://doi.org/10.1016/j.matchar.2007.06.003
24. Nandan R, Debroy T, Bhadeshia HKDH (2008) Recent advances in friction stir welding – process, weldment structure and properties. 53:980–1023
25. Schmidt HB, Hattel JH (2008) Thermal modelling of friction stir welding. Scr Mater 58:332–337. https://doi.org/10.1016/j.scriptamat.2007.10.008
26. Qiao GY, Xiao FR, Zhang XB et al (2009) Effects of contents of Nb and C on hot deformation behaviors of high Nb X80 pipeline steels. Trans Nonferrous Metals Soc China 19:1395–1399. https://doi.org/10.1016/S1003-6326(09)60039-X
27. Antonino T de S, Guimarães PB, Alécio R de A et al (2014) Measurements of the thermophysical properties of the API 5L X80. Mater Sci Appl 05:617–627. https://doi.org/10.4236/msa.2014.58064
28. Gadakh VS, Adepu K (2013) Heat generation model for taper cylindrical pin profile in FSW. Mater Sci Appl 2:370–375. https://doi.org/10.1016/j.jmrt.2013.10.003
29. De A, Bhadeshia HKDH, DebRoy T (2014) Friction stir welding of mild steel: tool durability and steel microstructure. Mater Sci Technol 30:1050–1056. https://doi.org/10.1179/1743284714Y.0000000534
30. Fratini L, Buffa G, Palmeri D et al (2006) Material flow in FSW of AA7075–T6 butt joints: numerical simulations and experimental verifications. Sci Technol Weld Join 11:412–421. https://doi.org/10.1179/174329306X113271
31. Lee SJ, Lee YK (2008) Prediction of austenite grain growth during austenitization of low alloy steels. Mater Des 29:1840–1844. https://doi.org/10.1016/j.matdes.2008.03.009
32. Zhang SS, Li MQ, Liu YG et al (2011) The growth behavior of austenite grain in the heating process of 300M steel. Mater Sci Eng A 528:4967–4972. https://doi.org/10.1016/j.msea.2011.02.089
33. Momeni A, Kazemi S, Ebrahimi G, Maldar A (2014) Dynamic recrystallization and precipitation in high manganese austenitic stainless steel during hot compression. Int J Miner Metall Mater 21:36–45. https://doi.org/10.1007/s12613-014-0862-4
34. Fairchild DP, Wasson AJ, Kumar A, et al (2012) Fractographic investigation of cleavage initiation in steel friction stir welds. In: Trends in welding research, 9th International Conference. pp 193–200
35. Li X, Shang C, Ma X et al (2017) Elemental distribution in the martensite–austenite constituent in intercritically reheated coarse-grained heat-affected zone of a high-strength pipeline steel. Scr Mater 139:67–70. https://doi.org/10.1016/j.scriptamat.2017.06.017